Article

## Advances in Preclinical PET Instrumentation

AMIRRASHEDI, Mahsa, ZAIDI, Habib, AY, Mohammad Reza

**Abstract**

In the light of ever-increasing demands for PET scanner with better resolvability, higher sensitivity and wide accessibility for noninvasive screening of small structures and physiological processes in laboratory rodents, several dedicated PET scanners were developed and evaluated. Understanding conceptual design constraints pros and cons of different configurations and impact of the major components will be helpful to further establish the crucial role of these miniaturized systems in a broad spectrum of modern research. Hence, a comprehensive review of preclinical PET scanners developed till early 2020 with particular emphasis on innovations in instrumentation and geometrical designs is provided.

Reference

**UNIVERSITÉ DE GENÈVE**

# Advances in Preclinical PET Instrumentation

Mahsa Amirrashedi[a,b], Habib Zaidi[c,d,e,f], Mohammad Reza Ay, PhD[a,b,*]

### KEYWORDS

- Small-animal PET imaging • Preclinical PET scanner • Instrumentation • Design • Performance

### KEY POINTS

- High-resolution PET scanners dedicated to preclinical studies facilitate the characterization of small details within the animal's body.
- Understanding the new trends in preclinical imaging will be helpful to further establish the crucial role of small-animal PET scanners in a wide spectrum of biomedical research activities.
- Detector material and design considerations are the most determinant factors affecting the PET scanner's overall performance.

## INTRODUCTION

Because of anatophysiological similarities between human and animal species, the use of animal models, particularly vertebrate mammals, has dramatically revolutionized many fields of modern research in basic biology, translational medicine, pharmaceutical industry, and several other areas.[1–3] Among numerous imaging modalities devoted to murine model investigations, PET rekindled a considerable interest due to gleaning a wealth of quantitative information about biological processes at the molecular and cellular levels.[4] Salient progress and considerable advances in small-animal PET imaging has had and will continue to have a far more profound effect on drug development and biomedical research. Ideally, a PET scanner dedicated to small laboratory animals would have to promise high-enough resolving power coupled to optimum detection efficiency to ensure visualization of a small amount of radiotracer uptake within microstructures of the animal body. In the light of ever-increasing demands for devices with better resolvability, a higher level of sensitivity, and wide accessibility for noninvasive screening of small structures and physiologic processes in laboratory rodents, the number of dedicated preclinical PET scanners is increasing rapidly. Preclinical PET scanners are gaining in importance, whereas concerns are surfacing over the design aspects as well as costs associated with software products and hardware developments. To conquer these limitations and challenges, a variety of dedicated small-animal PET prototypes, as well as commercial scanners with different configurations, architectural designs, and diversified types of software were characterized and evaluated during recent years. Although extensive research has been carried out on individual scanners, a comprehensive comparative assessment of the performance of different preclinical PET scanners is missing. This article aims to review advances in preclinical PET with particular emphasis on instrumentation until early 2020.

[a] Department of Medical Physics and Biomedical Engineering, Tehran University of Medical Sciences, Tehran, Iran; [b] Research Center for Molecular and Cellular Imaging, Tehran University of Medical Sciences, Tehran, Iran; [c] Division of Nuclear Medicine and Molecular Imaging, Geneva University Hospital, Geneva CH-1211, Switzerland; [d] Geneva University Neurocenter, Geneva University, Geneva CH-1205, Switzerland; [e] Department of Nuclear Medicine and Molecular Imaging, University of Groningen, University Medical Center Groningen, Groningen 9700 RB, Netherlands; [f] Department of Nuclear Medicine, University of Southern Denmark, Odense 500, Denmark
* Corresponding author, Department of Medical Physics & Biomedical Engineering, Tehran University of Medical Sciences, School of Medicine, Poursina Street, Tehran, Islamic Republic of Iran.
E-mail address: mohammadreza_ay@sina.tums.ac.ir

## BRIEF HISTORY OF PRECLINICAL PET SCANNERS

The early development of preclinical PET scanners dates back to mid-1990s when the first dedicated systems were developed following the same design principles used in human scanners. A more detailed history and characterization of the first animal scanners have been well-reviewed by Chatziioannou,[5] Goertzen and colleagues,[6] Levin and Zaidi,[7] and Tai.[8] However, to project the current trends and essential challenges in this era, a brief snapshot of the early designs adopted for animal studies is valuable. The first generation of specialized PET systems used large gantry apertures to accommodate medium-sized species, such as rhesus and squirrel monkeys as well as small rodents. The SHR-2000 scanner is one of the earliest designs explored by Hamamatsu (Hamamatsu, Japan)[9,10] ,which comprises Bismuth-Germinate (BGO) detectors arranged in four rings with 384 mm diameter and spatial resolution of 3 mm and 4.8 mm in the transaxial and axial directions, respectively. The viability of in vivo measurements in rat brain using a dual BGO block detector was initially reported by Rajeswaran and colleagues.[11] This was followed by the development of the first PET device dedicated to conscious brain imaging in rats.[12] This small tomograph, so-called RATPET, was based on 16 BGO detector blocks coupled to photomultiplier tubes (PMTs) arranged in a ringlike geometry with 115 mm diameter and 50 mm axial field-of-view (AFOV), which ultimately resulted in a transaxial resolution of 2.2 mm at the center of the field of view (CFOV).[12] The first Avalanche-photodiode (APD)-based scanner (Sherbrooke APD PET) consisted of 512 BGO crystals arranged in 2 rings such that the face-to-face distance between opposite detectors of the ring was 135 mm and the axial length was 10.5 mm. The scanner features a wobbling scheme and one-to-one coupling to improve the spatial resolution up to 2.1 mm at the CFOV. The first commercial platform adapted successfully for imaging small laboratory species are the microPET series developed by Concorde Microsystems Inc. (Knoxville, TN).[13] The first-generation microPET systems offered dedicated 4-ring versions for primates (P4) and rodents (R4) imaging with ring diameters of 261 and 148 mm, respectively.[14,15] Both configurations were composed of lutetium-oxyorthosilicate (LSO) scintillators forming a 78 mm axial length. The next-generation microPET series, including Focus-120, Focus-220, and the Inveon-DPET have also been marketed.[16–18] All microPET families developed by Siemens were based on

LSO/PSPMT detectors with further refinements in detector geometries, crystal dimensions, and electronics. The Inveon, the last design of the microPET series, is a trimodality platform offering the largest axial extension (127 mm), up to three-fold higher sensitivity (6.27%) in comparison to its predecessors.

The yttrium-aluminum-perovskite (YAP)-(S)PET scanner developed at the Universities of Ferrara and Pisa was a commercial model using four rotating heads with a 150 mm distance between opposite panels.[19] As its name implies, the scanner was based on YAP crystals. For simultaneous PET/SPECT imaging, one pair of the opposed detectors was set in coincidence mode to enable PET acquisition, whereas the second was operated as SPECT detectors equipped with low-energy high-resolution collimators. The use of PET or SPECT mode was also feasible. The reconstructed volumetric resolution in PET mode at the CFOV was 8.5 $mm^3$, with maximum absolute sensitivity of 1.87% for an energy window of 50 to 850 keV.

The only preclinical product marketed by Philips is the Mosaic-HP composed of pixelated lutetium-yttrium-orthosilicate (LYSO) crystals encoded by PMT-based readouts.[20] The transaxial FOV (TFOV) and axial FOV (AFOV) of the scanner were suitable for one-bed whole-body rodent imaging. The transaxial spatial resolution was 2.34 mm for a central point source with a 2.83% peak absolute photon sensitivity (385–665 keV).

Another fully engineered preclinical device (ClearPET) with adjustable rotating heads was manufactured by Raytest Isotopenmessgeraete GmbH (Mannheim, Germany). The scanner is made up of 20 rotating dual-layered LYSO/lutetium-YAP (LuYAP) detectors. The adjustable heads allowed forming TFOVs with 94 and 144 mm diameters and axial extension of 110 mm. The reconstructed spatial resolution and absolute photon sensitivity following NEMA-NU4 standards are 1.9 to 2 mm full-width at half maximum (FWHM) at 5 cm radial offset and 4.7% (100–750 keV), respectively.[21,22]

The FLEX Triumph is the first trimodality PET/SPECT/computed tomographic (CT) system introduced into the market by Gamma Medica-Ideas (Northridge, CA). The platform includes a 4-head SPECT subunit based on cadmium zinc telluride (CZT) detectors coplanar with the XO-CT scanner, integrated with the X-PET or LabPET8 subsystems. X-PET, the commercial version of Rodent Research PET (RRPET), is based on 16 BGO/PMT detector blocks, arranged in a pentagon shape to form a FOV with 200 mm width and 116 mm length. The large AFOV together with BGO-based crystals result in good sensitivity of

5.9% at CFOV when using 250 to 750 keV energy window.[23]

Another well-known family in the preclinical PET market is LabPET series commercialized by Gamma Medica/GE Healthcare.[24,25] LabPET family features phoswich detectors individually coupled to APD photodetectors. Three versions of the scanner, called LabPET4, LabPET8, and LabPET12, with an equivalent ring diameter of 162 mm and axial extensions of 37.5, 75, and 115 mm were released by the company.[24,26] The LabPET scanners comprise dual-layered tapered LYSO/ lutetium-gadolinium oxyorthosilicate (LGSO) phoswich detectors with side-by-side readout electronics to cope with the parallax-error associated with small ring diameters.

SEDECAL (Madrid, Spain) has also offered different commercial designs with finer crystal elements in comparison to the abovementioned systems. One of them incorporated LYSO/GSO crystals backed by PSPMTs known as Argus (eXplore Vista), whereas the second one (VrPET/CT) is a coplanar PET/CT scanner based on V-shaped LYSO detector blocks arranged in a partial ring geometry with a rotating gantry.[27,28] The other coplanar design manufactured by the same company is the rPET-1 composed of 2 rotating planar heads with 45 mm AFOV and TFOV. In comparison to other versions of the rPET scanners with two double-block heads, the rPET-1 suffers from 2-fold lower sensitivity. The small crystal pitches used on the rPET-1 resulted in 1.4-mm spatial resolution at the CFOV following NEMA-NU4 protocols.[21] For the widest energy window available on the scanner (100–700 keV), the highest achievable sensitivity was 1%.

## STATE-OF-THE-ART PRECLINICAL PET SCANNERS

The remarkable improvements in system designs and overall performance introduced by the different vendors resulted in the current generation preclinical PET scanners surpassing the previous generations in many aspects (**Fig. 1**, **Table 1**). Because of space constraints, the general features of each model (evaluated after 2012) is briefly discussed in this section. Detailed information about various designs along with system performance tests following NEMA NU 4-2008 procedure[22] are also summarized in **Tables 2** and **3**.

Recently, Mediso Medical Imaging Systems (Budapest, Hungary) came up with a wide range of multimodality in vivo solutions, including Nano-PET/CT, nanoScan PET/MR imaging, and Nano-PET/SPECT/CT platforms as well as other bimodal techniques, such as SPECT/CT and SPECT/MR imaging. Except for the magnet shielding in PET/MR imaging combination, the PET component in NanoScan family is identical, which consists of fine LYSO pixels arranged around a 180-mm ring enabling sequential PET and CT acquisitions via NanoPET/CT or in-line PET and MR imaging (1T) via nanoScan PET/MR imaging.[29,30] The AFOV and TFOV of the units are sufficiently large (95 and 123 mm, respectively) to encompass the entire body of rodents. Another specific and highly versatile design released by Mediso is the MultiScan LFER 150 PET/CT, which is particularly adapted for dynamic brain imaging in awake nonhuman primates (NHPs) in recumbent and sitting positions.[30,31]

The IRIS PET from Inviscan (Strasbourg, France) represents the latest generation of commercial small-animal scanners operating either in rotating or stationary modes.[32] In bimodal PET/CT mode, the PET module is placed at the back of the CT unit and could rotate around the scanned objects to acquire high-quality images in step and shoot modes with 95 mm coverage in the axial direction.[32]

The Albira triple-modality system is an integrated SPECT/PET/CT platform manufactured by Bruker Oncovision (Valencia, Spain) in the form of a single-, dual-, and triple-ring models.[33–35] All versions feature the same TFOV (80 mm) but different axial extensions (~46, 94.5, and 148 mm). The system is integrated with a high-resolution CT and SPECT subsystems sharing a common gantry. The SPECT detectors are based on (CsI(Na)) with adjustable FOVs and mounted in a coplanar configuration with the CT unit. Albira is the first revolutionary design commercially available based on monolithic LYSO detectors instead of pixelated crystals to circumvent parallax issue and achieve a highly uniform spatial resolution across the scanner FOV. The first generation of Albira was based on PSPMT readout, whereas the next-generation detectors were made up of LYSO crystals readout by high-density silicon photomultipliers (SiPMs) arrays (Si detectors), which in turn facilitates integration as a PET insert for simultaneous PET/MR imaging.[36,37] PET/CT Si78 is a new high-performance bimodal technology introduced by Bruker.[37] Si78-PET subsystem is identical to the Albira Si with an extended AFOV (up to 149–200 mm) and a seamless integration with a low-dose high-resolution CT subsystem. With 10-layered depth of interaction (DOI) encoding capability coupled to SiPM technology, Si detectors deliver supreme spatial resolution along the scanner's FOV for accurate quantification.

Unlike conventional PET scanners, MILabs VECTor (Utrecht, Netherlands) exploits a

**Fig. 1.** Range of state-of-the-art PET scanners dedicated to preclinical imaging. *Courtesy of* the owner companies.

completely different concept for detecting annihilation photons. The scanner is equipped with 192 clustered pinholes collimator attached to 3 NaI(Tl)-based stationary heads generating a triangular shape to surround the object. Each pinhole has a diameter of 0.7 mm with 16° to 18° opening angle, making the detection of annihilation photons in single mode feasible.[38,39] Its specific design enables imaging of co-injected radiotracers to perform concurrent PET/SPECT acquisition with submillimeter spatial resolution.[40]

PETbox is a benchtop prototype built specifically for imaging laboratory mice with dual head detectors on a static gantry.[41] PETbox 4 is the upgraded version, made up of 4 stationary heads with a dimension of 5 × 10 cm$^2$ forming a TFOV of 44 mm and AFOV of 98 mm.[42] This compact low-cost design is well-suited for whole-body mouse imaging. Another central feature of the scanner is the use of BGO scintillators, which improves the scanner's detection capability for low-dose studies up to 18.1% with a default window of 150 to 650 keV.

BGO crystals have also been implemented on G-series (G4, G8, and GNEXT) commercialized by Sofie Biosciences (CA, USA).[43–45] As the name suggests, G4 is composed of 4 detector modules in a boxlike geometry, whereas the number of transaxial modules is increased up to 8 in its upgraded G8 version to effectively cover the gap areas. In addition, there are several hardware refinements that improve G8 performance in comparison to G4, including scintillator dimensions, light guide designs, and acquisition electronics.[43] Another key difference is the integration mode. G8 is a sequential integrated PET/CT, whereas G4 version is supplied with x-ray projection and optical photographic images to gather complementary anatomic templates for PET images. With submillimeter spatial resolution and peak absolute sensitivity of 9% at the CFOV, G8 is among the latest generation high-performance preclinical PET scanners. At the time of writing this review, Sofie unveiled the latest member of G-series family, GNEXT PET/CT, with DOI measurement capability by using LYSO/BGO phoswich detectors. By incorporating this unique feature, GNEXT achieves 12% sensitivity and less than 1 mm spatial resolution at the CFOV with 120 mm TFOV and axial length of 105 mm.[45]

Inliview-3000 is a trimodal SPECT/PET/CT imaging scanner developed at the Tsinghua University (China).[46] All subunits are mounted on the same gantry and sharing a common animal chamber. The scanner features the same LSO/PMT ring for either PET or SPECT imaging modes integrated with a cone-beam CT module. The PET unit has 50 and 100 mm TFOV and AFOV, respectively. Switching to SPECT acquisition is applicable by an add-on collimator with 50 elliptical pinholes. The average spatial resolution of the scanner operating in PET mode is 2.12 mm FWHM at the CFOV with 3.2% peak sensitivity for a 250 to 750 keV energy window.

β-cube from MOLECUBES (Gent, Belgium) is one of the most intuitive and unique bench-tops exploiting monolithic LYSO crystals coupled to SiPMs.[47,48] The system has a TFOV of 72 mm

**Table 1**
**Design characteristics of PET scanners dedicated for preclinical studies**

| Scanner | Manufacturer | Scintillator | Crystal Dimensions (mm$^3$) | Electronic | Crystal Pitch (mm) | Gantry Aperture (mm) | TFOV (mm) | AFOV (mm) | DOI Capability |
|---|---|---|---|---|---|---|---|---|---|
| microPET P4[6,14] | Siemens | LSO (8 × 8) | 2.2 × 2.2 × 10 | PSPMT | 2.45 | 220 | 190 | 78 | NO |
| microPET R4[6,15] | Siemens | LSO (8 × 8) | 2.1 × 2.1 × 10 | PSPMT | 2.45 | 120 | 100 | 78 | NO |
| microPET Focus-120[6,17] | Siemens | LSO (12 × 12) | 1.51 × 1.51 × 10 | PSPMT | 1.59 | 120 | 100 | 76 | NO |
| microPET Focus-220[6,16] | Siemens | LSO (12 × 12) | 1.51 × 1.51 × 10 | PSPMT | 1.59 | 220 | 190 | 76 | NO |
| Inveon-DPET[6,18,100] | Siemens | LSO (20 × 20) | 1.51 × 1.51 × 10 | PSPMT | 1.59 | 120 | 100 | 127 | NO |
| Mosaic-HP[6,20] | Philips | GSO | 2 × 2 × 10 | PMT | 2.3 | 197[a] | 128 | 119 | NO |
| Argus(eXplore Vista)[6,27] | Sedecal | LYSO/GSO (13 × 13)/ (20 × 20) | 1.45 × 1.45 × 7/8 | PSPMT | 1.55 | 80 | 67 | 48 | YES |
| ClearPET[6,21] | Raytest GmbH | LYSO/LuYAP (8 × 8)/ (8 × 8) | 2 × 2 × 10/10 | PSPMT | 2.3 | 135/220[a] | 94/144 | 110 | YES |
| rPET-1[21] | Sedecal | MLS | 1.4 × 1.4 × 12 | PSPMT | 1.5 | 140[a] | 45.6 | 45.6 | NO |
| VrPET[28] | Sedecal | LYSO (30 × 30) | 1.4 × 1.4 × 12 | PSPMT | 1.5 | 140[a] | 86.6 | 45.6 | NO |
| LabPET4[25] | Gamma Medica | LYSO/LGSO | 2 × 2 × 11.9/13.3 | APD | NA | 162[a] | 100 | 37 | YES |
| LabPET8[6,24] | Gamma Medica | LYSO/LGSO | 2 × 2 × 11.9/13.3 | APD | NA | 162[a] | 100 | 75 | YES |
| LabPET12[6,26] | Gamma Medica | LYSO/LGSO | 2 × 2 × 11.9/13.3 | APD | NA | 162[a] | 100 | 112.5 | YES |
| X-PET[23] | Gamma Medica | BGO (8 × 8) | 2.32 × 2.32 × 9.4 | PMT | NA | 165[a] | 100 | 116 | NO |
| NanoPET/CT[30,111] | Mediso | LYSO (39 × 81) | 1.12 × 1.12 × 13 | PSPMT | 1.17 | 160 | 123 | 94.8 | NO |
| NanoScan PET/MRI[29,111] | Mediso | LYSO (39 × 81) | 1.12 × 1.12 × 13 | PSPMT | 1.17 | 160 | 120 | 94 | NO |
| nanoScan (PET82S)[111] | Mediso | LYSO (29 × 29) | 1.51 × 1.51 × 10 | NA | NA | 110 | 80 | 98.6 | NO |
| LFER 150[59] | Mediso | LYSO (29 × 29) | 1.51 × 1.51 × 10 | NA | NA | 260 | 200 | 150 | NO |
| Albira[35] | Bruker | LYSO[b] | 50 × 50 × 10 | MAPMT | Monolithic | 111 | 80 | 46 | YES |
| Albira[33] | Bruker | LYSO[b] | 50 × 50 × 10 | MAPMT | Monolithic | 111 | 80 | 94.5 | YES |
| Albira[90] | Bruker | LYSO[b] | 50 × 50 × 10 | MAPMT | Monolithic | 111 | 80 | 148 | YES |
| Albira Si[36] | Bruker | LYSO[b] | 50 × 50 × 10 | SiPMs | Monolithic | NA | 80 | 148 | YES |
| PETbox[41] | UCLA | BGO (20 × 44) | 2 × 2 × 5 | PSPMT | 2.2 | 50 | 44 | 96.8 | NO |
| PETbox4[42] | UCLA | BGO (24 × 50) | 1.82 × 1.82 × 7 | PSPMT | 1.9 | 50 | 45 | 95 | NO |

(*continued on next page*)

**Table 1**
(*continued*)

| Scanner | Manufacturer | Scintillator | Crystal Dimensions (mm$^3$) | Electronic | Crystal Pitch (mm) | Gantry Aperture (mm) | TFOV (mm) | AFOV (mm) | DOI Capability |
|---|---|---|---|---|---|---|---|---|---|
| G4[44] | Sofie Biosciences | BGO (24 × 50) | 1.8 × 1.8 × 7 | MAPMT | 1.83 | 50 | 45 | 94 | NO |
| G8[43] | Sofie Biosciences | BGO (26 × 26) | 1.75 × 1.75 × 7.2 | MAPMT | 1.83 | 50 | 47.44 | 94.95 | NO |
| GNEXT[45] | Sofie Biosciences | LYSO/BGO (8 × 8)/(8 × 8) | 1.01 × 1.01 × 6.1 1.55 × 1.55 × 8.9 | NA | NA | 139 | 120 | 104 | YES |
| ClairvivoPET[53] | Shimadzu | LYSO/LYSO (32 × 53)/ (32 × 54) | 1.28 × 2.68 × 7 | PMT | 1.4 × 2.8 | 182 | 102 | 151 | YES |
| TransPET-LH[50] | Raycan | LYSO | 1.89 × 1.89 × 13 | PSPMT | 2.03 | 192[a] | 130 | 53 | NO |
| Trans-PET/CT X5[51] | Raycan | LYSO (13 × 13) | 1. 9 × 1.9 × 13 | NA | NA | 160 | 130 | 50 | NO |
| Xtrim-PET[55] | Parto Negar Persia | LYSO (24 × 24) | 2.1 × 2.1 × 10 | SiPMs | 2.1 | 166 | 100 | 50.3 | NO |
| IRIS[32] | Inviscan SAS | LYSO (27 × 26) | 1.6 × 1.6 × 12 | MAPMT | 1.69 | 100 | 80 | 95 | NO |
| β-cubes[47] | Molecubes | LYSO[b] | 25 × 25 × 8 | MPPC | Monolithic | 76[a] | 72 | 130 | YES |
| VECTor[39] | MILabs | NaI(Tl)[b] | NA | NA | Monolithic | NA | 48 | 36 | YES |
| MuPET[56] | University of Texas M.D. Anderson Cancer Center | LYSO (30 × 30) | 1.24 × 1.4 × 9.5 | PMT | NA | 166 | 100 | 116 | NO |
| Eplus-260[59] | Chinese Academy of Sciences. | LYSO (16 × 16) | 1.9 × 1.9 × 10 | PSPMT | 2 | 263[a] | 190 | 64 | NO |
| MiniEXPLORER[60] | EXPLORER Consortium and Siemens Medical solutions | LYSO (13 × 13) | 4 × 4 × 20 | PMT | NA | 435[a] | 320 | 457 | NO |
| MiniEXPLORER II[61] | EXPLORER Consortium and Siemens Medical solutions | LYSO (6 × 7) | 2.76 × 2.76 × 18.1 | SiPMs | 2.85 | 520[a] | NA | 483 | NO |

*Abbreviations:* MLS, mixed lutetium silicate; NA, not available.
  [a] Ring diameter.
  [b] Monolithic crystal.

**Table 2**
**Spatial resolution of preclinical PET scanners**

| Scanner | Radial FWHM (mm) | Volumetric Resolution (mm$^3$) | Reconstruction Method |
|---|---|---|---|
| microPET P4[6] | 2.29 at 5 mm | 10.9 at 5 mm | FORE + FBP |
| microPET R4[6] | 1.65 at center<br>2.13 at 5 mm | 12.8 at 5 mm | FORE + FBP |
| microPET Focus-120[6] | 1.18 at center<br>1.92 at 5 mm | 6 at 5 mm | FORE + FBP |
| microPET Focus-220[6] | 1.75 at 5 mm | 5.35 at 5 mm | FORE + FBP |
| Inveon-DPET[6] | 1.63 at 5 mm | 6.33 at 5 mm | FORE + FBP |
| Mosaic-HP[6] | 2.7 at center<br>2.32 at 5 mm | 14.2 at 5 mm | 3DRP |
| Argus(eXplore Vista)[6] | 1.63 at 5 cm | NA | 2DFBP |
| ClearPET[6,21] | 1.94 at 5 mm<br>1.9 at 5 mm | 12.16 at 5 mm | 3DFBP |
| rPET-1[6] | 1.4 at 5 mm | 4 at 5 mm | SSRB + FBP |
| VrPET[6,21] | 1.48 at center<br>1.52 at 5 cm | 6.54 at 5 mm | SSRB + FBP |
| LabPET4[25] | 1.42 at center | NA | MLEM + SRM |
| LabPET8[6] | 1.7 at center<br>1.65 at 5 mm | 7.5 at center | SSRB + FBP |
| LabPET12[26] | 1.65 at 5 mm | NA | SSRB + FBP |
| X-PET[23] | 2 at center | 12 at center | FORE + FBP |
| NanoPET/CT[30] | 1.03 at center | 1.19 at center | SSRB + FBP |
| NanoScan PET/MRI[29] | 1.28 at center<br>1.5 at 5 mm | 1.8 at 5 mm | SSRB + FBP |
| LFER 150[31] | 1.81at 5 cm | 5.06 at 5 mm | FORE + FBP |
| Albira 1 ring | 1.55 at center<br>1.65 at 5 mm | 4.45 at center<br>5.52 at center | SSRB + FBP |
| Albira 2 ring[33] | 1.78 at center<br>1.92 at 5 mm | 7.5 at center<br>6.46 at 5 mm | SSRB + FBP |
| Albira 3 ring | 1.55 at center | 4.45 at center | SSRB + FBP |
| Albira Si[36] | 0.89 at center | ~ 1 within whole FOV | MLEM + DOI |
| PETbox[41] | 1.61 at central<br>  coronal plane x<br>1.54 at central<br>  coronal plane y<br>2.61 anterior-<br>  posterior | 6.63 at center | MLEM |
| PETbox4[42] | 1.32 at center | 3.4 at center | 3D MLEM |
| G4[44] | ~1.35 at center | NA | MLEM |
| G8[43] | <1 at center<br><1 at 5 mm | <1 at center<br><1 at 5 mm | MLEM |
| ClairvivoPET[53] | 2.16 at 5 cm | 13 at 5 mm | FORE + FBP |
| TransPET-LH[50] | 0.95 at center | 1 at center | 3D OSEM |
| Trans-PET/CT X5[51] | 2.11 at center | 5.72 at center | SSRB + FBP |
| Xtrim-PET[55] | 2.01 at 5 mm | 6.81 at center | SSRB + FBP |
| IRIS[32] | 1.05 at 5 mm | 1.38 at 5 mm | 3DMLEM |
| β-cubes[47] | 1.06 at center | ~1 | 3DFBP |
| VECTor[39] | NA | NA | NA |

**Table 2**
**(continued)**

| Scanner | Radial FWHM (mm) | Volumetric Resolution (mm³) | Reconstruction Method |
|---|---|---|---|
| MuPET[56] | 1.25 at center<br>1.48 at 5 mm | 1.34 at center<br>1.96 at 5 mm | SSRB + FBP |
| Eplus-260[59] | 1.68 mm at 5 mm | 3.71 at 5 mm | SSRB + OSEM + PSF |
| MiniEXPLORER[60] | 3 at center | ~ 27 at center | 3D list mode OSEM + TOF |
| MiniEXPLORER II[61] | 2.6 within 10 mm from center[a] | NA | FORE + FBP |

*Abbreviations:* FBP, filtered back projection; FORE, fourier rebinning; MLEM, maximum-likelihood expectation maximization; NA, not available; OSEM, ordered subset expectation maximization; PSF, point spread function; SRM, system response matrix; SSRB, single-slice rebinning.
  [a] Average spatial resolution within 10 mm CFOV based on NEMA NU 2-2012 standard.

and AFOV of 130 mm to easily accommodate small laboratory rodents in a compact and lightweight design. Regarding performance evaluation of the scanner, 1-mm³ volumetric resolution has been achieved due to 5-layered DOI capability of the monolithic detectors. The sensitivity for (435-588) and (255-765) keV energy windows are 5.7% and 12.4%, respectively.

The Trans-PET BioCaliburn is a highly modular and flexible preclinical PET series introduced by Raycan Technology (Suzhou, China) and available as LH, SH, and SH2 models with different AFOV and TFOV adapted to the user's requirements.[49,50] SH and SH2 modes have smaller TFOV (65 mm) in comparison to LH model (130 mm). The main difference between SH and SH2 models is the axial span of the detectors, which is twice for SH2 (106 mm). All models are constructed using LYSO arrays with $1.89 \times 1.89 \times 13$ mm³ crystal size with ~1 mm spatial resolution at the CFOV. A newer bimodal imager manufactured by Raycan, referred to as Trans-PET/CT X5 system with optimization in the firmware, was recently installed and evaluated.[51,52] The system has 130 mm TFOV, similar to the LH model, with a shorter AFOV (50 mm) and full digital electronics.

Among all commercial systems, the largest AFOV (151 mm) belongs to ClairvivoPET manufacturer by Shimadzu (Kyoto, Japan).[53,54] The system is based on a dual-layered LYSO detection scheme arranged to form a TFOV with 102 mm diameter and equipped with $^{137}$Cs transmission source for attenuation correction. Because of the large AFOV, the system outperforms most of the commercial series with an absolute sensitivity of 8.72% using a 250 to 750 keV energy window.[53]

Xtrim-PET is a cost-effective and high-modular porotype design based on SiPM technology from Parto Negar Persia (Tehran, Iran). The single-ring version of the scanner consists of 10 LYSO block detectors with 100 mm TFOV and 50.4 mm AFOV. The effective AFOV can be extended up to 195 mm for whole-body rodent imaging and multibed reconstruction. This compact and portable design offers ~2 mm spatial resolution and 2.99% peak detection efficiency at the CFOV for a 250 to 650 keV energy window.[55]

MuPET/CT developed at the University of Texas M.D. Anderson Cancer Center is a low-cost high-performance prototype based on PMT.[56] Of note in this design is the block-detector production methodology called slab-sandwich-slice. Each sandwich is made up of 13 attached LYSO slabs. After cutting sandwiches into slices, 13 slices were stacked together to make a block. In order to form a gap-free detection ring, the end crystals of each block are tapered with 6° to achieve 95% packing fraction. The system offers a 6.38% sensitivity for a 350 to 650 keV energy window.

SuperArgus PET/CT family, the latest version from SEDECAL, is the first real-time PET imager enabling on-line position adjustment using a time stamp technique. SuperArgus systems use state-of-the-art phoswich technology with expandable TFOV and AFOV to enable scanning objects with different size, ranging from mice to primates.[57]

Recently, four different configurations of preclinical PET models were designed by MR Solutions (UK) allowing standalone, simultaneous, and sequential PET/CT or PET/MR imaging. All the available models (MRS*PET/CT benchtop, MRS*PET/CT80, MRS*PET/CT120, MRS*PET/CT220) feature the same detector assemblies of multilayered (LSO/PMT) detectors with parallax-correcting capability and submillimeter (<0.8 mm) spatial resolution.[58]

**Table 3**
**Results of NEMA-NU4 2008 performance evaluation along with energy and temporal resolutions for preclinical PET scanners**

| Scanner | TW (ns) | ER (%) | TR (ns) | Peak Absolute Sensitivity (%)[a] | NECR-Mice (kcps) | NECR-Rat (kcps) | SF-Mice (%) | SF-Rat (%) |
|---|---|---|---|---|---|---|---|---|
| microPET P4[6,14] | 6 | 26 | 3.2 | 1.19 (350–650) | 601[g] | 173 | 5.2 | 16.7 |
| microPET R4[6,15] | 6 | 23 | NA | 2.06 (350–650) | 618 | 164 | 9.3 | 22.2 |
| microPET Focus-120[6,17] | 6 | 18.3 | NA | 3.42 (350–650) | 897 | 267 | 5.6 | 20.3 |
| microPET Focus-220[6,16] | 6 | 18.5 | NA | 2.28 (350–650) | 763[g] (250–700) | 359 | 7.2 | 19.3 |
| Inveon-DPET[6,18,100] | 3.4 | 14.6 | 1.22 | 6.72 (350–625) | 1670 | 592 | 7.8 | 17.2 |
| Mosaic-HP[6,20,69] | 7 | 17 | NA | 2.83 (385–665) | 555 | 244 | 5.4 | 12.7 |
| Argus (eXplore Vista)[6,27] | 7 | 26/33 (LYSO/GSO) | ~1.3 | 4.32 (250–700) | 117 | 40 | 21 | 34.4 |
| ClearPET[6,21] | 12 | 25/28 (LuYAP/LYSO) | 2 | 4.7 (100–750) 3.03 (250–650) | 73.4 (250–750) 73 (250–650) | NP | 31 (250–650) | NP |
| rPET-1[21] | 3.8 | NA | NA | 1 (100–700) | 29.2 (250–650) | NP | 24.2 | NP |
| VrPET[6,28] | 3.8 | 16.5 | NA | 1.56 (250–650) 0.94 (400–700) 2.22 (100–700) | 74 (100–700) | 31 | 11.5 | 23.3 |
| LabPET4[25] | 20 | 24/25 | 6.6 (LYSO/LYSO) 8.9 (LGSO/LYSO) 10.7 (LGSO/LGSO) | 1.1 (250–650) | 129 | 72 | 17 | 29 |
| LabPET8[6,24,25] | 20 22 10/15/20[b] | 24/25 | 6.6 (LYSO/LYSO) 8.9 (LGSO/LYSO) 10.7 (LGSO/LGSO) | 2.36 (250–650) 1.33 (250–650) 2.1 (250–650) | 279 183 (250–650) | 94 67 | 15.6 19 | 29.5 31 |
| LabPET12[6,26] | 20 | 19/20 | 7.1 (LYSO/LYSO) 8.3 (LGSO/LYSO) 9.2 (LGSO/LGSO) | 5.4 (250–650) | 362 | 156 | 16 | 29.3 |
| X-PET[23] | 12 | NA | NA | 5.9 (250–750) 9.3 (350–650) | 106 (250–750) | 49 | 7.9 | 21 |
| NanoPET/CT[30] | 5 | 19 | 1.5–3.2 | 7.7 (250–750) | 430 | 130 | 15 | 30 |
| | 5 | 19 | 1.5–3.2 | 8.4 (250–750) | 406 | 119 | 17.30 | 34 |

*(continued on next page)*

**Table 3**
(*continued*)

| Scanner | TW (ns) | ER (%) | TR (ns) | Peak Absolute Sensitivity (%)[a] | NECR-Mice (kcps) | NECR-Rat (kcps) | SF-Mice (%) | SF-Rat (%) |
|---|---|---|---|---|---|---|---|---|
| NanoScan PET/MRI[29] | | | | | | | | |
| LFER 150[31] | 5 | 3.3–5.4 | NA | 3.3 (400–600) 5.4 (250–750) | NP | 398 (400–600) | NP | 14 |
| Albira 1ring | 5 | 18 | NA | 2 (358–664) 2.5 (255–767) | 16.9 (358–664) | 12.8 | 7.5 | 13 |
| Albira 2 ring[33] | 5 | 18 | NA | 4.18 (358–664) 5.3 (255–767) | 72 (255–767) | 42 | 9.8 | 21.8 |
| Albira 3 ring | 5 | 18 | NA | 6.3 (358–664) | NA | NA | NA | NA |
| Albira Si[36] | NA | 15 | NA | 9 (256–767) | 576 (256–767) | 330 | NA | NA |
| PETbox[41] | 20 | 20.1 | 4.1 | 3.99 (150–650) | 20 (150–650) 18.2 (250–650) | NP | 21.3 (150–650) 14.3 (250–650) | NP |
| PETbox4[42] | 20 | 18 | 4.1 | 18.1 (150–650) | 35 | NP | 28 | NP |
| G4[44] | 20 | 18 | NA | 14 (150–650) | NP | NP | NP | NP |
| G8[51] | 20 | 19.3 | NA | 9 (350–650) 17.8 (150–650) | 44 (350–650) | NP | 11 | NP |
| ClairvivoPET[53,54] | 10 | NA | NA | 8.7 (250–750) | 415 (250–750) | NP | 17.7 | NA |
| TransPET-LH[50] | 5 | 13 | 1.5 | 2.4 (250–750) 2.04 (350–650) | 110 (250–750) 62 (350–650) | 40 25 | 11 8.4 | 19.3 17.7 |
| Trans-PET/CT X5[51] | 5 | 15 | NA | 1.7 (350–650) | 126 (350–650) | 61 | 14 | 24 |
| Xtrim-PET[55] | 10 | 12 | 1.8 | 2.2 (400–700) 2.99 (250–650) | 113.18 (250–650) | 82.76 | 12.5 | 25.8 |
| IRIS[32] | 5.2 | 14 | 2.6 | 8 (250–750) 6.6 (350–750) | 185 (250–750) | 40 | 15.6 | 22.4 |
| β-cubes[47] | 5 | 12 | NA | 5.7 (435–588) 8[d] (385–640) 12.4 (255–765) | 300 (435–588) 325[d] (385–640) 300[d] (255–765) | 160 (435–588) 162[d] (385–640) 140[d] (255–765) | 11.3 (435–588) | 15.7 (435–588) |
| VECTor[39] | NA | NA | NA | 0.31 | NA | NA | NA | NA |
| MuPET[56] | 3.4 | 14 | 600 ps | 6.38 (350–650) | 1100 | 354 | 12 | 28 |

| | | | | | | | |
|---|---|---|---|---|---|---|---|
| Eplus-260[59] | 2 | NA | NA | 1.8 (360–660) | NP | 26.5[e] | NP | 34.2[e] |
| MiniEXPLORER[60] | 3.6 | NA | 609 ps | 5[f] (425–650) | NP | 1741[e] | NP | 16.5[e] |
| MiniEXPLORER II[61] | 2.7–2.9 | 11.7 | 409 ps | 51.8 (kcps/MBq)[c] (430–1000) | NP | 1712[e] | NP | 19[e] |

Abbreviations: ER, energy resolution; NA, not available; NECR, noise equivalent count rate; NP, not performed; SF, scatter fraction; TR, temporal resolution; TW, timing window.

[a] Energy window setting used for sensitivity and NECR evaluations are shown in parenthesis.
[b] LYSO-LYSO/LYSO-LGSO/LGSO-LGSO.
[c] Data were measured following NEMA NU 2-2012 standards.
[d] Approximated values estimated from the curves in the cited reference.
[e] Results were reported for monkey-like phantom.
[f] Data were measured following NEMA NU 2-2007 standards.
[g] Peak NECR value is not reached due to insufficient activity in the FOV.

Several scanners were designed specifically for NHP imaging. The Eplus-260 primate PET was recently constructed by the Institute of High Energy Physics, Chinese Academy of Sciences. This scanner used LYSO/PSPMT detection modules offering an extra-large bore (230 mm) and axial coverage (64 mm) allowing PET scanning of larger objects.[59] The reconstructed spatial resolution was measured to be 1.8 mm within the 50 mm TFOV with 1.8% sensitivity using a 360 to 660 keV energy window.

MiniEXPLORER I and II were developed by the EXPLORER Consortium in collaboration with Siemens Medical solutions (Knoxville, TN).[60,61] LSO/PMT detector modules of Siemens Biograph mCT clinical PET scanner model was redesigned to build MiniEXPLORER I total-body primate imager.[60] The scanner has an aperture of 435 mm and an AFOV of 475 mm, leading to 15% sensitivity and ~3 mm spatial resolution at the CFOV following NEMA NU 2-2012 standards [62] the second version of the scanner, Mini-EXPLORER II was also adopted for veterinary applications and human brain imaging.

## DESIGN CONSIDERATIONS AND PERFORMANCE CHARACTERIZATION OF PRECLINICAL PET SCANNERS
### Detector Material and Conceptual Design Considerations

It has long been known that the emergence of LSO scintillators in 1992 revolutionized the PET imaging portfolio in various aspects.[63] MicroPET scanner series was the first enjoying the superior benefits of LSO arrays.[13] Among all types of scintillator materials used in PET scanners, L(Y)SO scintillators are still the materials of choice due to their outstanding characteristics in terms of density (7.4 g/cm$^3$), effective atomic number (Z = 66), light output (75%), and decay constant (40 ns).[7] However, the major drawback of these scintillators is the intrinsic radiation emitted from Lutetium-176 with 202 and 307 keV prompt gamma photons, which limits the minimum amount of the activity detectable by the scanner. This might be an issue in low-dose studies, such as cell tracking or gene expression research.[64] Moreover, lutetium background activity is not deemed critical in clinical imaging but could affect image quality, particularly in compact small bore scanners, such as miniaturized preclinical machines that implement wider energy windows due to lower injected activities. Although by increasing the lower level of energy discriminator (LLD) up to 350 keV one could eliminate single photons emitted from Lutetium background, the summed energy of single photons could still cover the photopeak window and degrade the contrast of PET images. The contribution of these photons is dictated by the amount of lutetium used in the scanner design and system geometry. For instance, the intrinsic count rate is about 4 cps for VrPET,[65] 186 kcps for NanoPET/MR imaging,[29] and 145 kcps for Hyperion $\Pi^D$ insert.[66] Albeit these limitations, background photons could be used in daily quality control of the detectors, energy calibration, DOI extraction, PET-CT registration, and also time-of-flight (TOF) applications in clinical PET scanners.[67] Other scintillation materials, such as BGO, have been widely used in the early generation of preclinical PET scanners owing to its high atomic number (Z = 83) and photofraction of 41.5% at 511 keV, yielding higher detection capability in a more compact and costless design. YAP crystals were also used in early designs such as YAP-(S)PET and Tier-PET scanners.[19,68] Although YAP crystal presents better temporal properties, it was not considered a good candidate owing to its lower detection efficiency. Other scintillation materials such as LuYAP have been used in conjunction with LYSO in ClearPET phoswich detectors. LGSO and GSO crystals have also found interest in phoswich arrays, such as SuperArgus and Lab-PET models.

GSO scintillator has also been investigated in the APET scanner, the prototype version of Philips Mosaic-HP. However, after 6 months it was substituted by LSO owing to inferior properties of GSO, particularly in terms of light yield and density.[20,69] Performance comparison of APET(LSO) and APET(GSO) under the same testing conditions proved that scintillator choice affects different aspects of scanner performance. Because LSO crystal generates around 3.75 times more photons than GSO, better crystal identification and thus narrower FWHM and full-width at tenth-maximum were achieved for APET(LSO). Measurements using a $^{68}$Ge line source have been shown as good as twice higher sensitivity and noise equivalent count rate (NECR) for APET(LSO).

As mentioned earlier, the chemical composition of the scintillator directly influences many aspects of system performance, such as detection efficiency, energy resolution, time resolution, and counting rate performance. These effects will be discussed in the following sections in more detail. The other key factor that should be taken into account when devising a small-animal scanner is the shape of the detector arrangements. Unlike clinical scanners, commonly adopting cylindrical geometries, various designs were proposed for small-animal PET scanners to push the limitations

for spatial resolution and sensitivity, including stationary multipanel (VECTor, PETbox), rotating multihead (rPET-1, YAP(S)PET, VrPET), rotating ring (ClearPET, IRIS PET/CT), boxlike arrangement (G-series, PETbox4), and polygon or ringlike orientation, which are the most prevailing configurations for full-ring models. The multihead configuration could be used more efficiently in dual-purpose PET/SPECT acquisitions such as YAP(S)PECT and VECTor models, but such design suffers from low geometric efficiency and imaging artifacts regarding lower packing fraction. Further concerns that may arise with the multihead scheme is head misalignment, which hinders ultimate image quality as well as quantitative accuracy. According to simulation studies, the best design to maximize detection efficiency is boxlike configuration.[70] Scanners with polygon layout manifest a nonuniform pattern of resolution degradation across the transaxial FOV in contrast to ringlike cylinders owing to dead regions in polygon designs generated by arranging rectangular blocks around an annulus that negatively affects system efficiency and uniformity.[55,66,71]

The type of light sensor used to measure the scintillator output is as, if not more, important than scintillation crystals in determining overall scanner's performance. Among the many alternatives available, including PMTs, position-sensitive PMTs (PSPMTs), and multichannel PMTs (MC-PMTs), APDs, and SiPMs; are the default choices in PET devices intended for small-animal imaging.[72] The bulky size of conventional PMTs renders them unsuitable for one-to-one coupling, particularly in high-resolution scanners with small crystal arrays. However, PSPMTs composed of multiple anodes with individual outputs that share a common glass tube provide more accurate spatial information regarding their structure. Although most of the preclinical scanners are still based on PSPMTs, PET inserts benefit from superior advantages of MR imaging–compatible solid-state photosensors, such as APDs and SiPMs.[66,71,73,74] For the first time, APDs have been used on the Sherbrooke PET scanner and its successor, the LabPET. These photodiode detectors offer a multitude of advantages over PMTs, including small size, lower cost, and magnetic tolerance. The small dimensions of APDs in comparison to PMTs enable one-to-one coupling in high-performance scanners, which in turn improves spatial and energy resolution of the scanner. However, the downsides of APD photosensors are the small gain and inferior timing properties that make them less tempting in preclinical applications. The inherent

limitations of APDs were addressed by the introduction of Geiger mode APDs or SiPMs. These assemblies are refined versions of APDs with fine microcell arrays, called single-photon avalanche diodes (SPADs) operating in the Geiger regime. SiPMs boast favorable advantages relative to conventional PMTs, such as comparable intrinsic gain, minimal dark noise, compactness, immunity to magnetic and electric fields, and also lower price. SiPMs are now available both in analog and digital formats. In an analog SiPM, signals from individual SAPD cells are summed up to determine timing and energy information. However, in digital mode, the signal is produced in each micro-SAPD with its time-stamp information. Digital SiPMs give clear improvements in energy and temporal resolutions and also provide lower temperature sensitivity as opposed to analog counterparts. Hyperion $\Pi^D$ is the first preclinical model with digital SiPM readout electronics.[66]

In quest of submillimetric range resolution, the application of indirect room-temperature compound semiconductor detectors such as cadmium-telluride (CdTe) and CZT was also investigated.[7,75] Unlike scintillation-based detectors in which the spatial resolution is mainly limited by crystal element size, in semiconductor detectors, the intrinsic spatial resolution is determined by the fine pitch between adjacent electrodes. The fine structure imaging PET scanner developed at Tokyo university pioneered the use of CdTe detectors for high-resolution preclinical studies.[76] The system gantry was built out of 10 detection units around an annulus with 70 mm diameter and 26 mm axial coverage. Each detection unit consists of 2 detector layers of CdTe with a 0.6 mm offset to measure 3-dimensional (3D) position information. With such a design, the study found a 0.74 mm FWHM tangential resolution. Another ultra-high-resolution CZT-based PET scanner with 4-sided box geometry and selectable TFOV is under development at Stanford University.[75,77] The scanner provides 80 × 80 × 80 mm$^3$ FOV by using CZT detectors with 40 × 40 × 5 mm$^3$ dimensions in an edge-on configuration. These detectors are more compact in size and provide fine energy resolution (~3% at 511 keV) due to direct charge conversion process, superior packing fraction (~99%), and more importantly, ultrafine spatial resolution. Another factor reflecting the superiority of CZT over its scintillation counterpart is the capability of 3D event positioning to reduce the magnitude of the parallax error. There are however several technical concerns in using CZT in

PET, including poor timing resolution and lower atomic number.[7]

### Spatial Resolution

Spatial resolution is the finest detail that can be resolved by a PET scanner, which is a function of several compounding factors. These include pixel pitch size, positron range, noncollinearity of annihilation photons, ring diameter, detector readout, coupling scheme, and image reconstruction algorithm. The spatial resolution of a PET system is primarily governed by the detector element size.[78] The conventional crystal element size in animal scanners is approximately less than 1.5 to 2 mm. Although this resolution meets the basic requirements for rat imaging, it is not sufficient for divulging fine details in the mice.[5] Ignoring the physical factors, the best achievable empirical spatial resolution equals to half the pitch size between adjacent detector elements. Therefore, the most straightforward approach to improve PET's spatial resolution without sacrificing detection capability is incorporating minuscule but lengthy crystal elements. The main limitations associated with such design are poor light collection efficiency and parallax error, which is more dominant in close geometries.[7] These issues lead to the use of relatively shorter crystals in animal scanners (10∼13 mm) in comparison with those in clinical scanners. However, in current designs, such as PETbox prototypes and G-series, narrow crystals with 5 mm and 7.5 mm thicknesses were used taking advantage of the high absorption efficiency of BGO crystals, which ultimately preserves photon collection ability while minimizing parallax contribution in a close-packed layout. The other elegant advantage of box geometry is the equivalent propagation of the penetration effect across the system's FOV known as parallax error.[43]

Over the years, different innovative methods were investigated to alleviate parallax phenomena (Fig. 2), at least partly, by measuring the interaction point within each crystal element. The most conventional and practical one is using multilayer crystals to allocate each event to the actual interaction depth. Some commercial scanners, such as ClairvivoPET, and newly developed prototype models, such as MADPET4 and MRS-PET, are based on dual-layered offset arrays of LYSO/LYSO pairs.[53,71,74] Several investigators extended this approach to 4 layers and even 8 layers of detectors.[79,80] The initial investigations of 4-layered LSO detectors by single-side readout pattern specialized for small-animal jPET-RD proved the feasibility of the method.[79] The alternative depth encoding technique is incorporating phoswich

design compromised of multilayered crystals with different scintillation materials, such as (LYSO/LuYAP) in the ClearPET, (LYSO/LGSO) in LabPET series, (LYSO/GSO) in SuperArgus, and (LYSO/BGO) in GNEXT, where the DOI information is obtained from the differences in decay times between the layers. Because in the multilayered approach the accuracy of DOI assessment is directly determined by the number of detector layers and the thickness of each layer, the method is less effective in small-bore PET scanners.[27,53] Moreover, the multilayer paradigm bears several penalties, such as increasing the design complexity and electronic channels as well as out-of-FOV scattered photons, which is the main source of scattered radiation in preclinical setting. NEMA-based evaluation of preclinical PET scanners proved the increased contribution of scattered photons in multilayered systems.[6] Another popular technology to implement continuous DOI information is dual-end readout. In this case, two photosensors are placed at both ends of each crystal element. The ratio of the signal amplitude generated in each photosensor allows the determination of the depth of photon's impact. It has been shown that this technique facilitates a DOI resolution of ∼2 mm using PSAPDs.[81] In a follow-up study, a dedicated brain mice prototype was developed based on tapered crystals read out from both ends using PSPADs.[82] For this design, a DOI resolution of ∼1.5 mm was obtained by irradiating the crystals with a 1-mm width collimated beam. More recently, detector blocks with 0.5-mm LSO arrays with double-end SiPMs were fabricated to serve as building blocks of a high-resolution small-animal PET with DOI capability. With this configuration, a DOI accuracy of 1.84 mm FWHM was obtained.[83] A similar method was implemented in a new dual-ended PET insert with 48 detector blocks and AFOV of 106 mm. DOI resolution of 1.96 mm was measured for the insert composed of $1 \times 1 \times 20$ mm$^3$ LYSO crystals read out by SiPMs from each crystal end. Preliminary investigations of the PET insert indicated a uniform spatial resolution of 0.8 mm within the 50 mm of the scanner's TFOV with 15% sensitivity using an energy window of 250 to 750 keV.[83] The attenuation caused by the front photosensor, poor timing, and energy resolution, unavoidable gap regions between detection modules and twice more the number of photosensors are the major limitations of this readout technique. The most promising and cost-efficient solution seems to be continuous DOI encoding, which is feasible by means of monolithic crystal slabs. Monolithic crystals grasped attention in the market of dedicated scanners due to their excellent 3D positioning
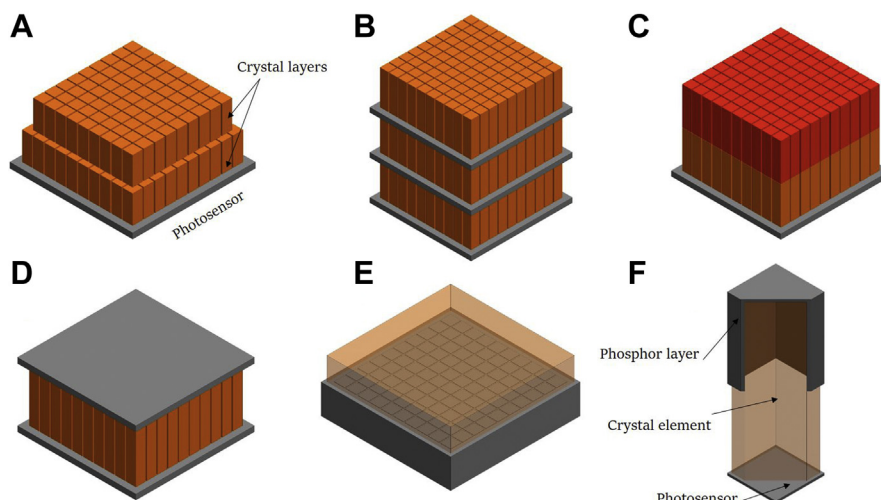
Fig. 2. Strategies for depth of interaction encoding. Dual-layered arrays with relative offset (*A*), Direct depth of interaction encoding using multiple crystal layers read out individually (*B*), Phoswich detectors compromised of multi-layered crystals with different scintillation materials (*C*), Dual-ended readout method (*D*), Monolithic crystal (*E*), phosphor-coating approach (*F*).

properties, easy and inexpensive production process, and high packing ratio.[34,47] The main concern of continuous crystals is the challenging calibration process to measure the hit position. Using a 5-layer DOI measurement, a DOI resolution of 1.6 mm was achieved for the β-cube scanner.[47] To extract the DOI information in the β-cube, a maximum likelihood algorithm was developed to achieve depth-dependent light spread function. DOI encoding in Albira detection slabs is based on the width of the light distribution, which becomes narrower as the interaction point gets closer to the photodetector. Another ongoing design using monolithic slabs is the DigiPET scanner tailored for rodent brain imaging.[84] The proposed design used LYSO slabs with $32 \times 32 \times 5$ mm$^3$ dimensions optically assembled with digital SiPMs. The scanner has 4-sided box geometry generating $32 \times 32 \times 32$ mm$^3$ FOV. For event positioning in DigiPET, a collimated 0.4-mm pencil beam was used. The variance of the light distribution following the irradiation of monolithic crystal with the pencil beam was used to extract DOI information. With such a design, a spatial resolution of 0.6 mm, DOI resolution of 1.6 mm, energy resolution of 23%, and coincidence time resolution of 529 ps were obtained. A different methodology enabling continuous DOI encoding is the phosphor-coating approach.[85] In this method, one face of the crystal is coated by a thin layer of phosphor material, which could absorb the scintillation light and re-emit depth-dependent phosphor light with some delay, whereas the other end of the crystal is coupled

to the photodetector. The light reaching the photodetector surface is a mixture of the scintillation light and delayed phosphor light. If a gamma photon strikes close to the photodetector, the amount of light received by the photosensor has a short decay time. However, if the photon hits the crystal far away from the photodetector, most of the photons detected by the photosensor are phosphor-emitted lights with long decay time.

Unlike polygon and ring orientations, the radial FWHM in dual-head scanners decreases toward the edges of the TFOV, which arises from the small number of detected events at the periphery of TFOV due to the absence of detector elements in these regions.[68] Therefore, the number of oblique line of responses (LORs) passing the center is more than in the edge regions, which consequently impairs the spatial resolution at the scanner's CFOV.

Spatial resolution blurring is affected not only by the radial distance from the center of the TFOV but also by the axial position of the object. Results from different studies indicated that the spatial resolution in the axial center is poorer than one-fourth offset due to a significant number of slanted LORs passing through the center. The effect is more pronounced for scanners with large AFOV.[18,53] As is the case with the radial resolution, deterioration of the axial spatial resolution is highly likely to occur in large axial spans as a consequence of DOI phenomena in the axial axis of the scanner. This nonuniformity is hampered by rebinning techniques before 2D reconstruction. As demonstrated on the Inveon-DPET scanner, the

axial spatial resolution depends on the maximum ring difference,[18] increasing the MRD from 1 to 79 leads to 0.8 mm deterioration of axial resolution. By selecting small ring differences while incorporating a 2D reconstruction scheme or using full 3D reconstruction methods, one could achieve a more homogenous spatial resolution within the whole AFOV. Although the effect of noncollinearity is less significant in small bore preclinical scanners, the FWHM broadening due to positron range effect is directly related to the type of radiotracer injected to the animal body and may contribute to resolution degradation, particularly when this range is larger than the scanner's intrinsic resolution. Several studies investigated the impact of positron range effect in small-animal imaging. Disselhorst and colleagues[86] performed a set of experiments to assess the effect of positron range on image quality metrics by scanning the NEMA quality phantom filled with several positron emitters. It has conclusively been shown that the finite positron range limits the overall spatial resolution in the Inveon-DPET. Similar results were obtained for microPET focus through imaging line sources filled with $^{18}F$, $^{19}N$, and $^{68}Ga$ embedded in a cylindrical phantom filled with tissue-equivalent materials. The results recognized the deleterious effect of positron range, particularly in low-density materials and long-range positron emitters.[87] Remarkable improvements in quantitative values were recently reported for [$^{68}Ga$] DOTA-labeled scan of mice by implementing positron range correction in the small-animal ARGUS PET/CT scanner.[88] Lastly, for high-resolution PET scanners with smaller aperture size and miniature detector elements, positron range is the dominant factor in FWHM blurring, whereas, for large-scale detector rings, noncollinearity of annihilated photons becomes more prominent.[89]

### Sensitivity

In PET imaging, the sensitivity refers to the minimum number of detected true events per unit of activity within the FOV. High-detection efficiency leads to a small but biologically more relevant amount of injected dose, rapid acquisition, lower motion artifacts, and hence higher visual quality of the resulting images. For the first-generation commercial PET scanners customized for murine studies, the sensitivity was less than ~5%, reaching about 18.1%, for the very latest generation (see **Table 3**). The overall sensitivity of a PET scanner is defined as a combination of geometric and intrinsic factors.[70] The geometric efficiency is determined with detector ring diameter as well as the axial length of the scanner, whereas the

intrinsic efficiency depends strongly on detector properties, packing fraction, and energy and time window settings. Scanners with a small radius and long axial FOV exhibit higher detection capability due to large solid angle coverage. State-of-the-art preclinical PET scanners have a wide range of ring diameters (50–250 mm) and axial FOV (45–151 mm) perfectly suitable for various applications. Decreasing the distance between the detectors and radioactive sources would increase the number of incident annihilation photons at the cost of increasing parallax-related errors. A different strategy would be to incorporate adjustable detector rings to fit the size of the scanned object as is the case with YAP(S)PET[19] and ClearPET.[21] Apart from the benefits, such designs come at the cost of additional mechanical complexity.

Increasing the number of axial rings to elongate the axial extension implies higher detection capability foremost but also facilitates whole-body imaging, a desirable feature for dynamic and gated studies. Furthermore, a long AFOV mitigates the nonuniformity problems associated with multibed reconstruction schemes. Most preclinical PET scanners have an axial FOV greater than 100 mm to cover a wide range of laboratory rodents in one session. Among the commercially available systems, the largest AFOV belongs to triple-ring Albira (148 mm), ClairvivoPET (151 mm), and Si78 (up to 149–200 mm).[37,53,90]

Aside from scanner geometry, several intrinsic factors compromise the number of detected annihilation events. Scintillation materials, such as BGO, with high stopping power and high effective atomic number increase the chance of photon absorption in each element by boosting the photoelectric absorption. Systems composed of BGO crystals provide higher peak efficiency even with shorter crystal elements less than 10 mm, compared to other systems with approximately equivalent axial coverage.[41,42,45] Increasing the thickness of detector elements would further enhance the possibility of photon absorption in each detector pixel but increases the positioning errors introduced by parallax, as explained earlier. The other determinant factor influencing system inherent sensitivity is the scanner packing, which is determined by the detector fill factor (active to the total area of the detector), interblock spacing, and inter-ring distance. The gap area between adjacent crystals occupied by reflective materials (to decrease intercrystal crosstalk) as well as dead zones between detection modules in polygon orientation would increase the number of undetected photons. Intermodular gaps not only decrease system sensitivity but also hinder image
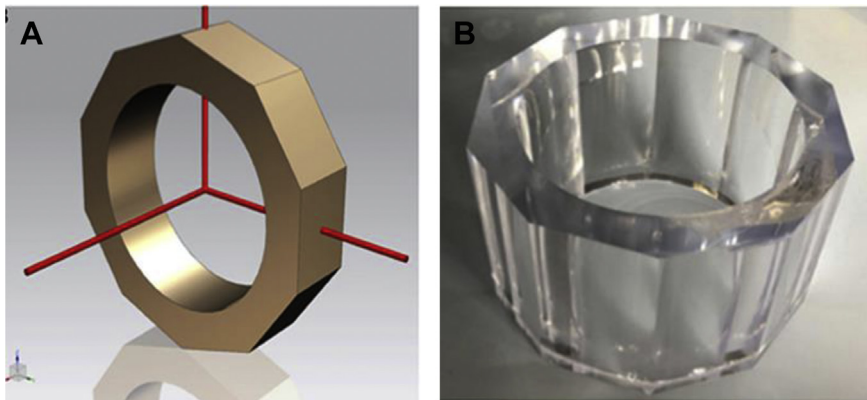
**Fig. 3.** Schematic view of a PET scanner based on single monolithic crystal ring (*A*) and manufactured monolithic LYSO tube (*B*). Reprinted from Gonzalez and colleagues[93] (The figure is licensed under Creative Commons Attribution 4.0 License).

quality by introducing starlike artifacts. The most conventional method to cover dead regions between adjacent modules consists increasing the number of transaxial detection blocks. This technique is reflected in G8 design by increasing the number of transaxial modules in contrast to its previous version (G4).[43] Moreover, using tapered shape crystals instead of conventional rectangular detection blocks yields further improvement in system sensitivity by filling the transaxial interblock gaps, as used in the X-PET subsystem of the FLEX Triumph model and the Albira scanner. This concept was previously investigated in Lab-PET systems through the use of trapezoid phoswich detectors, and also applied in newly developed scanners, such as the MuPET system. Monte Carlo simulations reported 60% enhancement in scanner sensitivity using tapered arrays instead of traditional cuboid models. Besides, experimental setups implied 11% degradation in spatial resolution when using tapered shaped crystals compared with rectangular crystals.[91] This effect is mainly attributed to increasing the crystal cross-section along the depth direction.[92]

A more elegant approach, called gapless PET was proposed more recently.[93] To build a gapless PET scanner, a monolithic PET tube is considered instead of individual detection blocks. The simulated scanner is made up of a monolithic LYSO tube (**Fig. 3**) with a cylindrical inner surface and a polygonal outer face to accommodate conventional pixelated SiPMs. Comparison of the proposed design with conventional polygonal multiblock PET (for the same geometry) indicated 20% reduction in production cost and 30% enhancement in system sensitivity and count rate capability of the scanner.[93] The same concept was also implemented by another group with

different geometric parameters. The simulated scanner, called AnnPET, enables 10% sensitivity achieved using a single LYSO annulus with 50 mm inner ring diameter and 72 mm axial extension.[94] However, a miniaturized PET imager has been constructed recently using a monolithic cylinder with 48.5 mm inner diameter and 5 mm length. The performance characterization of the scanner, called LOR-PET, is not available at the time of writing.[95]

Another important factor that will compromise the imaging performance is the homogeneity of the sensitivity profile along the z-axis of the scanner, which is controlled by the number of rings in the axial direction. Single-ring scanners offer more uniform profiles with a peak at the center of the detection ring, which drops linearly toward the edges of the AFOV, whereas the sensitivity profile of multiblock scanners deviate from typical behavior as a consequence of axial gaps between adjacent rings.[33,66] Additionally, in the single-ring orientation, the lack of axial uniformity may arise from block misalignment across the AFOV. This inhomogeneity could be mitigated by using more accurate normalization methods.[96]

Moreover, the number of detected events is affected by acquisition parameters, such as energy window, timing window settings, scan duration, and injected amount of radiotracer. Wider windows yield a drastically higher amount of photons accepted during acquisition at the expense of a higher percentage of unwanted random and scattered photons. For the G8 scanner, increasing the LLD from 150 to 350 keV with a fixed upper-level-discriminator shows about an 8% reduction in the scanner's central sensitivity.[43] For the β-cube scanner, the sensitivity increased by 2.17-fold when using (255-765 keV) energy window

instead of (435-588 keV).[47] Increasing the width of the timing window up to twice the system temporal resolution improves the system detection sensitivity, but further increases in the timing window seem not to have an additional effect on overall system sensitivity. Yang and colleagues[97] investigated the effect of timing window on the absolute sensitivity of the microPETⅡ scanner with 3 ns coincidence timing resolution. Their study has shown small dependency of scanner sensitivity with respect to timing windows beyond 10 ns. These findings were later confirmed by Kim and colleagues.[17] Another attractive and novel strategy to increase system sensitivity is Compton PET concept, which uses the kinematics of Compton scattering to recover scattered photons concerning the direction of entry of photons.[98,99] Similar to true events, the recovered scattered photons could then be used within the reconstruction process to boost the signal-to-noise ratio further. This could be achieved through CZT detectors with high energy and positioning resolution. The animal bed and other assemblies within the FOV could also compromise the scanner's sensitivity. To decrease the adverse effects of attenuation and scattering arising from the animal holder, the fiber Carbon bed is considered in some scanners, such as the microPET R4, NanoScan PET/MR imaging, Inveon-DPET, and Xtrim-PET scanners.

### Count-Rate Performance

The NECR is the most relevant metric indicating the system's ability to record true events relative to scattered and random coincidences. The overall counting performance of a PET device depends on a combination of factors, such as pulse pile-up, detector dead-time, signal resolving time, scintillator decay time, system sensitivity, object size, distribution of activity over the FOV, and acquisition parameters. To improve the signal-to-noise ratio and hence image quality, the injected activity should correspond to at least 90% to 95% the peak NECR of the scanner.

As a rule of thumb, higher detection efficiency leads to higher NECR but the relation is not trusted in all situations. For instance, some state-of-the-art scanners, such as PETbox4, G4, and G8 show high sensitivity but relatively low peak NECR, which is mainly due to undesirable temporal properties of BGO (300 ns decay time).[42–44] Crystals with short decay time, such as LSO, represents a more favorable count rate tolerance by reducing the chance of pile-up events. Further improvements in NECR could be achieved by incorporating electronic boards with lower noise and

shorter integration time. This issue is considered in MuPET design by developing special home-made pile-up event recovery channels in the FPGA board, which drastically ameliorates system counting behavior. The type of photodetector used to sense the scintillation light is of paramount importance in time resolution and detection throughput of the scanner. Systems with high temporal resolution peak at higher counting rate, such as the Inveon (1.22 ns, 1670 kcps),[100] MuPET (600 ps, 1100 kcps),[56] NanoPET (1–2 ns, 430 kcps),[30] NanoPET/MR imaging (1–2 ns, 406 kcps),[29] or fully digital systems, such as Hyperion $\Pi^D$ (605 ps, 483 kcps).

Most preclinical scanners have adopted light sharing readout methods to decrease the number of electronic channels and signal processing complexity. Compared to one-to-one coupling, systems with block detector designs and light sharing electronics are more susceptible to increased pile-up events at a high flux rate, because a large number of crystals fires every photosensor. To exemplify this point, one could compare LabPET12 with individual pixel readout to other scanners with similar geometry such as ClearPET. With the same energy window, LabPET12 represented ∼ 4 times better counting performance, which is partly ascribed to the individual readout scheme.[6]

As mentioned in the preceding section, systems with larger AFOV, small bore, and higher packing fraction saturate at higher NECR. The best examples to support this statement are microPET families. Increasing the packing fraction, extending the AFOV and improving readout electronics contribute to higher gain in NECR at low amount of activity, as achieved in the Inveon-DPET in comparison to its forerunners.[6,18] Moreover, the inverse effect of ring diameter on system count tolerance can be evidenced by comparing the Focus120 unit with Focus220 in which an increase in detector ring diameter up to 83% suggests 30% reduction in NECR. In LabPET scanners, a 50% increase in AFOV length results in a 30% improvement in peak NECR, at the expenses of only a 2% increase in the scatter fraction ratio. As expected, partial ring geometries present smaller NECR (<100 kcps) in comparison to more constrained designs.[6,21] A two-fold improvement in the number of detection modules in the VrPET scanner compared to rPET-1 version approximately doubles the NECR values.[28] Approximately similar improvements have been achieved for PETbox prototypes when shifting from dual-head model to 4-head box geometry.[41,42] In addition, lower NECR values were reported for PET/MR imaging inserts with small AFOV, such as MRS-PET

(61.9 kcps),[74] SimPET-S (42.4 kcps),[101] MADPET4 (29.0 kcps),[71] and the scanner reported by Stortz and colleagues[102] (20.8 kcps).

In addition to the abovementioned factors, other important parameters controlling the NECR properties of the scanner are the size of the object being imaged and the distribution of activity within the FOV. For larger objects, the NECR peaks more quickly. NEMA evaluation of preclinical scanners revealed that the peak NECR for a micelike phantom is higher than that of ratlike and monkeylike phantoms. This effect is mainly attributed to the increasing number of scattered and attenuated true events with increasing phantom diameter. The dependency of count rate characteristics on energy and time window settings was studied for several scanners. For the microFocus120 scanner, higher NECR and scatter ratio were achieved for wider energy and timing windows.[17] However, these variations are more pronounced for ratlike phantom compared with micelike phantom. Similar results were observed for the Trans-PET scanner. For micelike phantom, NECR values of 110 and 62 kcps were measured using 250 to 750 keV and 350 to 650 keV windows, respectively.[49] For the β-cube benchtop, 4% to 10% improvements in NECR were reported for (385-640 keV) energy window compared with (435-588 keV) settings.[47] Decreasing the LLD from 350 keV to 250 keV exhibits 2-fold enhancement in NECR magnitude measured in MADPET4.[71] In comparison, for the LabPET12, increasing the LLD from 100 to 200 keV improves the peak NECR of ratlike phantom from 141 to 179 kcps by limiting the scattered events. However, by further increasing the LLD (up to 350 keV), the NECR decreases to 90 kcps due to decreasing the number of true coincidences.[26] Reducing the width of the temporal window in the Mosaic-HP improves the scanner count performance without compromising detection sensitivity to true coincidence events.[69] Hence, the acquisition parameters should be adjusted according to the size of the object and scanner performance. For small objects, such as mice, one could benefit from wider energy windows to achieve higher sensitivity and NECR. However, for larger animals and multianimal imaging, highest NECR could be achieved through limiting energy and timing windows. From the NECR point of view, although the characteristics of preclinical scanners are different, almost all of them are adequate for the typical range of activity used in preclinical research (∼30 MBq).

### Energy and Temporal Resolution

The main parameter influencing the energy resolution is the number of light quanta collected from the scintillator, which in turn is driven by the scintillator light yield, crystal refraction index, doping material, crystal element size, the coupling material, the wavelength of the scintillator light, and the quantum efficiency of the photodetectors. Crystals with higher luminosity such as L(Y)SO exhibit better characteristics in terms of energy and timing resolution. To decrease the light loss and improve light collection efficiency, each scintillator element is enclosed by reflective materials. The other important factor is the refractive index of the crystalline composition. As the light guide between the scintillator and photosensor is conventionally made of glass, scintillators with lower refraction index, such as LSO and GSO (∼1.5), show better light collection properties through minimizing the refracted photons that occur at the crystal/light guide interface. Using improved light guides in the Inveon-DPET scanner resulted in 8% improvement in energy resolution compared with first-generation models (P4, R4).[18,100] Similar results were also observed in the G8 scanner. Incorporating pixelated light guides in G8 instead of the 1 mm clear glass used in G4 suggested considerable improvements in energy resolution.[43] The quantum efficiency of the photosensor is also of paramount importance to achieve better energy and timing performance by decreasing the amount of statistical noise.[103] To date, breaking the barrier of 11% energy resolution and <1 ns becomes possible thanks to impressive properties of LSO/SiPM detectors, which are becoming the common theme in next-generation application-specific systems.[47,55,66] Besides the factors mentioned above, multiplexing readout and light sharing techniques hinder the energy and temporal precision. Using one-to-one coupling would help to promote energy and temporal characterization by decreasing the light loss at photodetector junction.[104] In a more recent study, a new strategy was developed to improve light collection efficiency while preserving spatial resolution and sensitivity of the detector blocks. In this new design, four layers of LYSO slabs were stacked together, such that each layer was optically separated from the adjacent layers and read out by SiPM arrays from 4 sides, results in energy and timing resolution of 10.38% and 348 ps, respectively.[99] The type of doping material is also another pertinent issue. Several studies investigated the types of doping materials to determine the optimum concentration of co-doping. It was verified that 0.5 mol % Yb-doped LSO: Ce crystals offer 2-fold lower afterglow compared with LSO:Ce crystals.[105] Another study reported that Li doping improves the light yield of LSO:Ce by ∼20% while decreasing the scintillation decay time up to

42.1 ns.[106] There are also other parallel efforts in this context. It was demonstrated that 0.04% Ca co-doped LSO: Ce exhibits superior light output (35,000 photons/MeV) and shorter decay time (31 ns), rendering it the best choice for TOF-PET scanners.[107] In a further study, sub-100 ps time resolution was obtained for a $2 \times 2 \times 3$ mm$^3$ LSO:Ce co-doped 0.4% Ca.[108] energy and timing resolutions are significantly imposed by the detector element size.[104] As discussed earlier, the most prominent disadvantages associated with thin and long crystals are parallax error, decreased energy and timing resolutions. The former could be mitigated using DOI strategies, whereas the latter remains a challenge for low aspect ratio crystals used in high-resolution scanners. Several strategies were proposed to retain the energy resolution without the limiting design trade-offs present in low aspect ratio, such as side readout techniques. Moreover, through the emergence of indirect semiconductor detectors, superior energy resolution ($\sim$3% at 511 keV) is feasible. As mentioned earlier, high energy resolution allows efficient rejection of scattered events and thus improvement of image contrast.

Apart from the abovementioned factors, the temporal resolution of a PET scanner is mainly affected by all elements involved in the detection chain: the scintillation crystal, the photosensor, light guide, and other components of the processing electronics. Scintillators with short decay time coupled to photodetectors with fast temporal response (fast raising time, fast transition time, and high quantum efficiency) are the primary components affecting coincidence timing resolution.[109] Improved temporal resolution ensures efficient rejection of undesirable random coincidences, which adds background to emission data and hence counteracts the resulting image quality. It is worth noting that the advantages of improved energy and timing resolution will not be significant in rodent imaging due to the small fraction of scattered and random coincidences. Some of the recent designs specialized for moderate or large nonhuman primate animals, such as Hyperion $\Pi^D$, Eplus-260, and MiniEXPLORER I could benefit from improved timing resolution for TOF-PET reconstruction.[59,61,66] The TT-TOF project based on Silicon pixel sensors with 16 steplike modules is being developed,[110] which is expected ... is expected to achieve 30 ps time resolution using Silicon-Germanium (Si-Ge) amplifiers in the pixel sensor. As the temporal resolution continues to be improved, the impetus grows for unlocking TOF imaging in small-animal imaging that would not have been dreamt possible in the preclinical era.

## SUMMARY AND FUTURE TRENDS

Because of the poor performance of clinical PET scanners for scanning small animals, a tremendous effort put into designing dedicated PET systems with finer spatial resolution, higher detection capabilities, minimum cost, and easy accessibility to fulfill the basic requirements of in vivo imaging to support longitudinal and noninvasive scanning of animal models with high statistical power. Since its emergence, several dedicated PET scanners with various design features and characteristics were developed in academic and corporate settings to meet preclinical researchers' higher-than-ever expectations. Some of these systems are still at the prototype stage for further evaluations, whereas some of them are commercially available and installed in research laboratories. Therefore, an updated overview of these dedicated small-animal PET scanners is provided emphasizing recent advances instrumentation. The identified limitations and challenges may help to predict future directions and depict a more realistic roadmap for this miniaturized and small-scale systems. To precisely translate and correlate the preclinical findings to clinical outcomes, around 0.5 mm spatial resolution is desired. Today, high-end state-of-the-art technologies approach submillimetric spatial resolution, breaking a barrier that could open the door to more specific applications and more accurate quantification by eliminating the partial volume issue. However, there are still ongoing efforts in this era to achieve more uniform volumetric resolution and consistent performance across the whole active volume of the scanner at a lower price. In this direction, cost-efficient monolithic slabs will continue to gain in popularity. The same can be expected for full digital SiPM photodetectors, which hold promises toward next-generation multimodality scanners, such as hybrid PET/MR imaging scanners. It should be mentioned that improved crystalline materials or more novel compositions and co-doping agents along with more advanced readout electronics may be available in the foreseeable future, which permits to incorporate TOF capability in state-of-the-art animal scanners. It is envisaged that more novel configurations, such as monolithic crystal rings, will foster a new era for high-performance scanners at a lower cost. However, the challenges of such designs are still not realized. It seems that direct semiconductor detectors, such as CZT, will continue to push themselves into commercial systems. In the light of these detectors, next-generation models will likely become available in a more concise fashion, particularly for more

specialized tasks, such as dedicated brain imagers for awake and behaving mice, which is eminently desirable in neuroscience studies. It should be emphasized that in addition to hardware design, there is still much that needs to be done in terms of fast, accurate, and reliable image reconstruction techniques. Research efforts are still required to evaluate and optimize current reconstruction algorithms and tuning acquisition settings for a variety of applications. Increasing demands for kinetic modeling, as well as high throughput imaging, will highlight the less noticed but significant role of quantitative corrections in preclinical settings as well. Although much effort is geared toward developing highly efficient scanners for preclinical research, still there is ample room for further improvements to save cost, time, and improved noise-resolution tradeoffs.

## ACKNOWLEDGMENTS

## REFERENCES

1. Cuccurullo V, D Di Stasio G, Schillirò ML, et al. Small-animal molecular imaging for preclinical cancer research: μPET and μSPECT. Curr Radiopharm 2016;9(2):102–13.
2. Epstein F, Catana C, Tsui B, et al. Small-animal molecular imaging methods. J Nucl Med 2010;51(0 1):18S–32S.
3. Toyohara J, Ishiwata K. Animal tumor models for PET in drug development. Ann Nucl Med 2011;25(10):717–31.
4. Phelps ME. Positron emission tomography provides molecular imaging of biological processes. Proc Natl Acad Sci USA 2000;97(16):9226–33.
5. Chatziioannou AF. PET scanners dedicated to molecular imaging of small animal models. Mol Imaging Biol 2002;4(1):47–63.
6. Goertzen AL, Bao Q, Bergeron M, et al. NEMA NU 4-2008 comparison of preclinical PET imaging systems. J Nucl Med 2012;53(8):1300–9.
7. Levin CS, Zaidi H. Current trends in preclinical PET system design. PET Clin 2007;2(2):125–60.
8. Tai YC, Laforest R. Instrumentation aspects of animal PET. Annu Rev Biomed Eng 2005;7:255–85.
9. Watanabe M, Uchida H, Okada H, et al. A high resolution PET for animal studies. IEEE Trans Med Imaging 1992;11(4):577–80.
10. Watanabe M, Okada H, Shimizu K, et al. A high resolution animal PET scanner using compact PS-PMT detectors. IEEE Trans Nucl Sci 1997;44(3):1277–82.
11. Rajeswaran S, Bailey DL, Hume S, et al. 2D and 3D imaging of small animals and the human radial artery with a high resolution detector for PET. IEEE Trans Med Imaging 1992;11(3):386–91.
12. Bloomfield P, Rajeswaran S, Spinks T, et al. The design and physical characteristics of a small animal positron emission tomograph. Phys Med Biol 1995;40(6):1105.
13. Cherry SR, Shao Y, Silverman R, et al. MicroPET: a high resolution PET scanner for imaging small animals. IEEE Trans Nucl Sci 1997;44(3):1161–6.
14. Tai Y-C, Chatziioannou A, Siegel S, et al. Performance evaluation of the microPET P4: a PET system dedicated to animal imaging. Phys Med Biol 2001;46(7):1845.
15. Knoess C, Siegel S, Smith A, et al. Performance evaluation of the microPET R4 PET scanner for rodents. Eur J Nucl Med Mol Imaging 2003;30(5):737–47.
16. Tai Y-C, Ruangma A, Rowland D, et al. Performance evaluation of the microPET focus: a third-generation microPET scanner dedicated to animal imaging. J Nucl Med 2005;46(3):455–63.
17. Kim JS, Lee JS, Im KC, et al. Performance measurement of the microPET focus 120 scanner. J Nucl Med 2007;48(9):1527–35.
18. Kemp BJ, Hruska CB, McFarland AR, et al. NEMA NU 2-2007 performance measurements of the Siemens Inveon™ preclinical small animal PET system. Phys Med Biol 2009;54(8):2359.
19. Del Guerra A, Di Domenico G, Scandola M, et al. High spatial resolution small animal YAP-PET. Nucl Instrum Methods Phys Res A 1998;409(1–3):537–41.
20. Huisman MC, Reder S, Weber AW, et al. Performance evaluation of the Philips MOSAIC small animal PET scanner. Eur J Nucl Med Mol Imaging 2007;34(4):532–40.
21. Cañadas M, Embid M, Lage E, et al. NEMA NU 4-2008 performance measurements of two commercial small-animal PET scanners: ClearPET and rPET-1. IEEE Trans Nucl Sci 2010;58(1):58–65.
22. National Electrical Manufacturers Association. NEMA standards publication NU 4-2008: performance measurements of small animal positron emission tomographs. Rosslyn (VA): National Electrical Manufacturers Association; 2008. p. 1–23.
23. Prasad R, Ratib O, Zaidi H. Performance evaluation of the FLEX triumph X-PET scanner using the national electrical manufacturers association NU-4 standards. J Nucl Med 2010;51(10):1608–15.
24. Prasad R, Ratib O, Zaidi H. NEMA NU-04-based performance characteristics of the LabPET-8™ small animal PET scanner. Phys Med Biol 2011;56(20):6649.
25. Bergeron M, Cadorette J, Beaudoin J-F, et al. Performance evaluation of the LabPET APD-based

digital PET scanner. IEEE Trans Nucl Sci 2009;
56(1):10–6.

26. Bergeron M, Cadorette J, Bureau-Oxton C, et al.
Performance evaluation of the LabPET12, a large
axial FOV APD-based digital PET scanner. IEEE
Nucl Sci Symp Conf Rec (NSS/MIC) 2009;4017–21.

27. Wang Y, Seidel J, Tsui BM, et al. Performance eval-
uation of the GE healthcare eXplore VISTA dual-
ring small-animal PET scanner. J Nucl Med 2006;
47(11):1891–900.

28. Lage E, Vaquero JJ, Sisniega A, et al. VrPET/CT:
Development of a rotating multimodality scanner
for small-animal imaging. IEEE Nucl Sci Symp
Conf Rec 2008;4671–4.

29. Nagy K, Tóth M, Major P, et al. Performance evalu-
ation of the small-animal nanoScan PET/MRI sys-
tem. J Nucl Med 2013;54(10):1825–32.

30. Szanda I, Mackewn J, Patay G, et al. National Elec-
trical Manufacturers Association NU-4 perfor-
mance evaluation of the PET component of the
NanoPET/CT preclinical PET/CT scanner. J Nucl
Med 2011;52(11):1741–7.

31. Sarnyai Z, Nagy K, Patay G, et al. Performance
evaluation of a high-resolution nonhuman primate
PET/CT system. J Nucl Med 2019;60(12):1818–24.

32. Belcari N, Camarlinghi N, Ferretti S, et al. NEMA
NU-4 performance evaluation of the IRIS PET/CT
preclinical scanner. IEEE Trans Radiat Plasma
Med Sci 2017;1(4):301–9.

33. Pajak MZ, Volgyes D, Pimlott SL, et al. NEMA NU4-
2008 performance evaluation of Albira: a two-ring
small-animal PET system using continuous LYSO
crystals. Open Med J 2016;3(1):12–26.

34. Sánchez F, Orero A, Soriano A, et al. ALBIRA: a
small animal PET/SPECT/CT imaging system.
Med Phys 2013;40(5):051906.

35. Balcerzyk M, Kontaxakis G, Delgado M, et al. Initial
performance evaluation of a high resolution Albira
small animal positron emission tomography scan-
ner with monolithic crystals and depth-of-
interaction encoding from a user's perspective.
Meas Sci Technol 2009;20(10):104011.

36. González AJ, Aguilar A, Conde P, et al. Next gener-
ation of the Albira small animal PET based on high
density SiPM arrays. IEEE Nuclear Science Sympo-
sium and Medical Imaging Conference (NSS/MIC)
2015;1–4.

37. Bruker. True trimodal preclinical PET SPECT CT sys-
tem. 2020. Available at: https://www.bruker.com/
products/preclinical-imaging/nuclear-molecular-ima
ging/pet-spect-ct.html. Accessed March 20, 2020.

38. Walker MD, Goorden MC, Dinelle K, et al. Perfor-
mance assessment of a preclinical PET scanner
with pinhole collimation by comparison to a
coincidence-based small-animal PET scanner.
J Nucl Med 2014;55(8):1368–74.

39. Goorden MC, van der Have F, Kreuger R, et al.
VECTor: a preclinical imaging system for simulta-
neous submillimeter SPECT and PET. J Nucl Med
2013;54(2):306–12.

40. MILabs. MILabs simultaneous sub-mm PET-SPECT
opens new avenues for advanced research. 2020.
Available at: https://www.milabs.com/vector/. Ac-
cessed March 20, 2020.

41. Zhang H, Bao Q, Vu NT, et al. Performance evalu-
ation of PETbox: a low cost bench top preclinical
PET scanner. Mol Imaging Biol 2011;13(5):949–61.

42. Gu Z, Taschereau R, Vu N, et al. NEMA NU-4 per-
formance evaluation of PETbox4, a high sensitivity
dedicated PET preclinical tomograph. Phys Med
Biol 2013;58(11):3791.

43. Gu Z, Taschereau R, Vu NT, et al. Performance
evaluation of G8, a high-sensitivity benchtop pre-
clinical PET/CT tomograph. J Nucl Med 2019;
60(1):142–9.

44. Herrmann K, Dahlbom M, Nathanson D, et al. Eval-
uation of the Genisys4, a bench-top preclinical PET
scanner. J Nucl Med 2013;54(7):1162–7.

45. Sofie. GNEXT PET/CT. 2020. Available at: https://
sofie.com/a-hrefproductsproductsa.          Accessed
March 20, 2020.

46. Wei Q, Wang S, Ma T, et al. Performance evaluation
of a compact PET/SPECT/CT tri-modality system
for small animal imaging applications. Nucl Instrum
Methods Phys Res A 2015;786:147–54.

47. Krishnamoorthy S, Blankemeyer E, Mollet P, et al.
Performance evaluation of the MOLECUBES β-
CUBE—a high spatial resolution and high sensi-
tivity small animal PET scanner utilizing monolithic
LYSO scintillation detectors. Phys Med Biol 2018;
63(15):155013.

48. MOLECUBES. B-CUBE. 2020. Available at: http://
www.molecubes.com/b-cube/. Accessed March
20, 2020.

49. Zhu J, Wang L, Kao C-M, et al. Performance evalua-
tion of the trans-PET® BioCaliburn® SH system.
Nucl Instrum Methods Phys Res A 2015;777:148–53.

50. Wang L, Zhu J, Liang X, et al. Performance evalu-
ation of the Trans-PET® BioCaliburn® LH system:
a large FOV small-animal PET system. Phys Med
Biol 2014;60(1):137.

51. Teuho J, Han C, Riehakainen L, et al. NEMA NU 4-
2008 and in vivo imaging performance of RAYCAN
trans-PET/CT X5 small animal imaging system.
Phys Med Biol 2019;64(11):115014.

52. RAYCAN. All-digital small animal PET. 2019. Avail-
able at: http://ray-can.com/en/. Accessed March
20, 2020.

53. Sato K, Shidahara M, Watabe H, et al. Performance
evaluation of the small-animal PET scanner Clairvi-
voPET using NEMA NU 4-2008 standards. Phys
Med Biol 2015;61(2):696.

54. Mizuta T, Kitamura K, Iwata H, et al. Performance evaluation of a high-sensitivity large-aperture small-animal PET scanner: ClairvivoPET. Ann Nucl Med 2008;22(5):447–55.

55. Amirrashedi M, Sarkar S, Ghafarian P, et al. NEMA NU-4 2008 performance evaluation of Xtrim-PET: a prototype SiPM-based preclinical scanner. Med Phys 2019;46(11):4816–25.

56. Wong W-H, Li H, Baghaei H, et al. Engineering and performance (NEMA and animal) of a lower-cost higher-resolution animal PET/CT scanner using photomultiplier-quadrant-sharing detectors. J Nucl Med 2012;53(11):1786–93.

57. SEDECAL. SuperArgus PET/CT. 2020. Available at: https://www.scintica.com/products/superargus-sed ecal-pet-ct-preclinical-systems/. Accessed March 20, 2020.

58. MRSolutions. Preclinical imaging systems. 2020. Available at: https://www.mrsolutions.com/ products/imaging-systems/. Accessed March 20, 2020.

59. Pei C, Baotong F, Zhiming Z, et al. NEMA NU-4 performance evaluation of a non-human primate animal PET. Phys Med Biol 2019;64(10):105018.

60. Berg E, Zhang X, Bec J, et al. Development and evaluation of mini-EXPLORER: a long axial field-of-view PET scanner for nonhuman primate imaging. J Nucl Med 2018;59(6):993–8.

61. Lyu Y, Lv X, Liu W, et al. Mini EXPLORER II: a prototype high-sensitivity PET/CT scanner for companion animal whole body and human brain scanning. Phys Med Biol 2019;64:075004.

62. Nema NU. NU 2-2012 performance measurements of positron emission tomographs. Rosslyn (VA): National Electrical Manufacturers Association; 2012.

63. Melcher CL. Scintillation crystals for PET. J Nucl Med 2000;41(6):1051–5.

64. Goertzen AL, Suk JY, Thompson CJ. Imaging of weak-source distributions in LSO-based small-animal PET scanners. J Nucl Med 2007;48(10): 1692–8.

65. Lage E, Vaquero J, Sisniega A, et al. Design and performance evaluation of a coplanar multimodality scanner for rodent imaging. Phys Med Biol 2009; 54(18):5427.

66. Hallen P, Schug D, Weissler B, et al. PET performance evaluation of the small-animal Hyperion IID PET/MRI insert based on the NEMA NU-4 standard. Biomed Phys Eng Express 2018;4(6): 065027.

67. Rothfuss H, Moor A, Young J, et al. Time alignment of time of flight positron emission tomography using the background activity of LSO. IEEE Nuclear Science Symposium and Medical Imaging Conference (NSS/MIC) 2013;1–3.

68. Weber S, Herzog H, Cremer M, et al. Evaluation of the TierPET system. IEEE Trans Nucl Sci 1999; 46(4):1177–83.

69. Surti S, Karp JS, Perkins AE, et al. Imaging performance of A-PET: a small animal PET camera. IEEE Trans Med Imaging 2005;24(7):844–52.

70. Habte F, Foudray A, Olcott P, et al. Effects of system geometry and other physical factors on photon sensitivity of high-resolution positron emission tomography. Phys Med Biol 2007;52(13):3753.

71. Omidvari N, Cabello J, Topping G, et al. PET performance evaluation of MADPET4: a small animal PET insert for a 7 T MRI scanner. Phys Med Biol 2017;62(22):8671.

72. Lewellen TK. Recent developments in PET detector technology. Phys Med Biol 2008;53(17):R287.

73. Schug D, Lerche C, Weissler B, et al. Initial PET performance evaluation of a preclinical insert for PET/MRI with digital SiPM technology. Phys Med Biol 2016;61(7):2851.

74. Vrigneaud J-M, Mcgrath J, Courteau A, et al. Initial performance evaluation of a preclinical PET scanner available as a clip-on assembly in a sequential PET/MRI system. Phys Med Biol 2018;63(12): 125007.

75. Gu Y, Matteson J, Skelton R, et al. Study of a high-resolution, 3D positioning cadmium zinc telluride detector for PET. Phys Med Biol 2011;56(6):1563.

76. Ishii K, Kikuchi Y, Matsuyama S, et al. First achievement of less than 1 mm FWHM resolution in practical semiconductor animal PET scanner. Nucl Instrum Methods Phys Res A 2007;576(2–3): 435–40.

77. Abbaszadeh S, Levin CS. 3-D position sensitive CZT PET system: current status. IEEE Nuclear Science Symposium, Medical Imaging Conference and Room-Temperature Semiconductor Detector Workshop (NSS/MIC/RTSD) 2016;1–2.

78. Moses WW. Fundamental limits of spatial resolution in PET. Nucl Instrum Methods Phys Res A 2011; 648:S236–40.

79. Tsuda T, Murayama H, Kitamura K, et al. Performance evaluation of a subset of a four-layer LSO detector for a small animal DOI PET scanner: jPET-RD. IEEE Trans Nucl Sci 2006;53(1):35–9.

80. Inadama N, Murayama H, Tsuda T, et al. Optimization of crystal arrangement on 8-layer DOI PET detector. IEEE Nucl Sci Symp Conf Rec 2006;5: 3082–5.

81. Yang Y, Wu Y, Qi J, et al. A prototype PET scanner with DOI-encoding detectors. J Nucl Med 2008; 49(7):1132–40.

82. Yang Y, Bec J, Zhou J, et al. A prototype high-resolution small-animal PET scanner dedicated to mouse brain imaging. J Nucl Med 2016;57(7):1130–5.

83. Kuang Z, Wang X, Fu X, et al. Dual-ended readout small animal PET detector by using 0.5 mm

pixelated LYSO crystal arrays and SiPMs. Nucl Instrum Methods Phys Res A 2019;917:1–8.

84. España S, Marcinkowski R, Keereman V, et al. Dig-iPET: sub-millimeter spatial resolution small-animal PET imaging using thin monolithic scintillators. Phys Med Biol 2014;59(13):3405.

85. Du H, Yang Y, Glodo J, et al. Continuous depth-of-interaction encoding using phosphor-coated scintillators. Phys Med Biol 2009;54(6):1757.

86. Disselhorst JA, Brom M, Laverman P, et al. Image-quality assessment for several positron emitters using the NEMA NU 4-2008 standards in the Siemens Inveon small-animal PET scanner. J Nucl Med 2010;51(4):610–7.

87. Alva-Sánchez H, Quintana-Bautista C, Martínez-Dávalos A, et al. Positron range in tissue-equivalent materials: experimental microPET studies. Phys Med Biol 2016;61(17):6307.

88. Cal-Gonzalez J, Vaquero JJ, Herraiz JL, et al. Improving PET quantification of small animal [68 Ga] DOTA-labeled PET/CT studies by using a CT-based positron range correction. Mol Imaging Biol 2018;20(4):584–93.

89. Levin CS, Hoffman EJ. Calculation of positron range and its effect on the fundamental limit of positron emission tomography system spatial resolution. Phys Med Biol 1999;44(3):781.

90. Spinks T, Karia D, Leach M, et al. Quantitative PET and SPECT performance characteristics of the Albira Trimodal pre-clinical tomograph. Phys Med Biol 2014;59(3):715.

91. St James S, Yang Y, Bowen SL, et al. Simulation study of spatial resolution and sensitivity for the tapered depth of interaction PET detectors for small animal imaging. Phys Med Biol 2009;55(2):N63.

92. Yang Y, James SS, Wu Y, et al. Tapered LSO arrays for small animal PET. Phys Med Biol 2010;56(1):139.

93. Gonzalez AJ, Berr SS, Cañizares G, et al. Feasibility study of a small animal PET insert based on a single LYSO monolithic tube. Front Med 2018;5:328.

94. Stolin AV, Martone PF, Jaliparthi G, et al. Preclinical positron emission tomography scanner based on a monolithic annulus of scintillator: initial design study. J Med Imaging (Bellingham) 2017;4(1):011007.

95. Xie S, Zhao Z, Yang M, et al. LOR-PET: a novel PET camera constructed with a monolithic scintillator ring. IEEE Nuclear Science Symposium and Medical Imaging Conference (NSS/MIC) 2017;1–3.

96. Badawi RD, Marsden P. Developments in component-based normalization for 3D PET. Phys Med Biol 1999;44(2):571.

97. Yang Y, Tai Y-C, Siegel S, et al. Optimization and performance evaluation of the microPET II scanner for in vivo small-animal imaging. Phys Med Biol 2004;49(12):2527.

98. Yoon C, Lee W, Lee T. Simulation for CZT Compton PET (Maximization of the efficiency for PET using Compton event). Nucl Instrum Methods Phys Res A 2011;652(1):713–6.

99. Peng P, Judenhofer MS, Cherry SR. Compton PET: a layered structure PET detector with high performance. Phys Med Biol 2019;64(10):10LT01.

100. Magota K, Kubo N, Kuge Y, et al. Performance characterization of the Inveon preclinical small-animal PET/SPECT/CT system for multimodality imaging. Eur J Nucl Med Mol Imaging 2011;38(4):742–52.

101. Ko GB, Yoon HS, Kim KY, et al. Simultaneous multi-parametric PET/MRI with silicon photomultiplier PET and ultra-high-field MRI for small-animal imaging. J Nucl Med 2016;57(8):1309–15.

102. Stortz G, Thiessen JD, Bishop D, et al. Performance of a PET insert for high-resolution small-animal PET/MRI at 7 tesla. J Nucl Med 2018;59(3):536–42.

103. Surti S, Karp JS. Advances in time-of-flight PET. Phys Med 2016;32(1):12–22.

104. Cates JW, Levin CS. Advances in coincidence time resolution for PET. Phys Med Biol 2016;61(6):2255.

105. Starzhinskiy N, Sidletskiy OT, Tamulaitis G, et al. Improving of LSO (Ce) scintillator properties by co-doping. IEEE Trans Nucl Sci 2013;60(2):1427–31.

106. Wu Y, Tian M, Peng J, et al. On the role of Li+ co-doping in simultaneous improvement of light yield, decay time, and afterglow of Lu2SiO5: Ce3+ scintillation detectors. Phys Status Solidi Rapid Res Lett 2019;13(2):1800472.

107. Spurrier M, Szupryczynski P, Rothfuss H, et al. The effect of co-doping on the growth stability and scintillation properties of lutetium oxyorthosilicate. J Cryst Growth 2008;310(7–9):2110–4.

108. Nemallapudi MV, Gundacker S, Lecoq P, et al. Sub-100 ps coincidence time resolution for positron emission tomography with LSO: Ce codoped with Ca. Phys Med Biol 2015;60(12):4635.

109. Lecoq P, Auffray E, Brunner S, et al. Factors influencing time resolution of scintillators and ways to improve them. IEEE Trans Nucl Sci 2010;57(5):2411–6.

110. Bandi Y, Benoit M, Cadoux F, et al. The TT-PET project: a thin TOF-PET scanner based on fast novel silicon pixel detectors. J Instrum 2018;13(01):C01007.

111. Mediso medical imaging systems. nanoScan SPECT/CT/PET. 2016. Available at: http://www.mediso.com/products.php?fid52,11&pid590. Accessed March 20, 2020.